Citation for final published version:

Aqueel Ahmed, Abu Talha, Hou, Bo , Inamdar, Akbar I., Cha, SeungNam, Kim, Hyungsang and Im, Hyunsik 2019. Morphology engineering of self-assembled nanostructured CuCo2O4 anodes for lithium-ion batteries. Energy Technology 7 (7) , 1900295. 10.1002/ente.201900295

Publishers page: http://dx.doi.org/10.1002/ente.201900295

DOI:

Article type: Communication

Morphology engineering of self-assembled nanostructured $CuCo_2O_4$ anodes for lithium–ion batteries

Abu Talha Aqueel Ahmed,[a] *Bo Hou,*[b] *Akbar I. Inamdar,**[a] *SeungNam Cha,*[c] *Hyungsang Kim,**[a] *Hyunsik Im**[a]

[a]Division of Physics and Semiconductor Science, Dongguk University, Seoul 04620, South Korea

[b]Department of Engineering Science, University of Oxford, Parks Road, OX1 3PJ, UK

[c]Department of Physics, Sungkyunkwan University, Suwon, 16419, Republic of Korea

E–mail: akbarphysics2002@gmail.com, hskim@dongguk.edu, hyunsik7@dongguk.edu,

Keywords: Li–ion Batteries, $CuCo_2O_4$, hydrothermal growth, Morphology engineering, power–law analysis

Abstract

The electrochemical kinetics and output capacity of active electrode materials are significantly influenced by its surface structure. Here, we report the template–free morphological evolution of $CuCo_2O_4$, achieved by controlling the nucleation and growth rate during the hydrothermal process, and evaluate its anode performance. The charge transfer resistance and specific surface area of the fabricated $CuCo_2O_4$ anode films were influenced by the viscosity of the solvent used. The optimized mesoporous nanosheet anode exhibited a high specific discharge capacity (1547 mAh g^{-1}) at 0.1 A g^{-1} and an excellenet restoring capability (~ 91%); it retained 88% of the initial capacity with a coulombic efficiency of ~ 99% even after 250 discharge–charge cycles. The superior lithium ion energy storage performance of this anode was due to its electrochemically favorable porous two–dimensional morphology with large Brunauer–Emmett–Teller (BET) specific surface area and pore volume, resulting in enhanced Li^+ storage and intercalation property.

Introduction

At the present time, electrochemical energy conversion and storage is a prime area of research because of the significant possible implication for the large–scale utilization with remarkably fast recharging capacity, high energy and power density, and excellent long cycle life with good endurance property.[1–3] Lithium–ion batteries (LIBs) have been widely used in energy–storage devices for energy management, communication equipment, hybrid electric vehicles, portable electronics, and so on.[4–6] The theoretical capacity of graphite–based carbonaceous materials is 372 mAh g^{-1} in commercial and economically convenient LIBs having good electrochemical conductivity and excellent discharge–charge stability.[7–9]

However, the increasing power demand of current advanced technologies requires new LIB anode materials with low cost and excellent electrochemical performance, such as $NiCo_2O_4$, $CoFe_2O_4$, $ZnCo_2O_4$, and $CuCo_2O_4$ (CCO);[10–24] Table S1 (Supporting Information) compares the electrochemical performances of these active anode materials that were tested in LIBs with the present work.

The direct growth of self–supported ternary transition metal oxides on current–collecting substrates has been recently explored to overcome the drawbacks of mixing active electrode materials with binders and conductive additives, enhance the endurance and speed up the discharge–charge processes; in particular, $CuCo_2O_4$ (Figure 1) has exhibited good Li^+ storage properties since both anions contribute to the faradaic redox mechanism for electrochemical energy storage.[25–32] However, $CuCo_2O_4$–based anodes suffer from large volume change upon cycling, causing drastic capacity fading that results in a short discharge–charge cycle life. Moreover, their poor rate performance due to the inherent slow conversion kinetics must be improved to attain a superior restoration capability. The Li^+ storage properties of anode materials can be enhanced by improving the ionic and electronic conductivity as well as increasing the electrochemically active sites.[33] The latter can be achieved via the morphology engineering of the anode material because specific individual morphologies hold their own specific surface areas, which influence their Li^+ storage properties. In general, complex template–assisted techniques are involved in modifying the anode size and shape, but the resulting physical properties are still unstable, weakening the endurance performance.[27,30] Therefore, a strategy for the fabrication of novel anode materials having specific surface areas maximized via morphology engineering, without losing other material properties, should be developed. In addition, three–dimensional (3D) network structures of active materials can allow a large surface area for reactions and open channels for an efficient ion–electron transport, which are both important properties for their use in LIBs.[25]

In the present study, we demonstrate the binder–free, shape–controlled, and single–step synthesis of $CuCo_2O_4$ on a Ni foam current collector via a mild hydrothermal method using different solvents. This work provides a novel outlook and understanding of the delivered specific capacity of $CuCo_2O_4$–based anodes. The surface structure of the anode material notably influenced their output capacity and electrochemical kinetics. An optimized nanosheet $CuCo_2O_4$ anode exhibited remarkable Li^+ storage properties (first specific discharge capacitiy of 1547 mAh g^{-1} at a current density of 100 mAh g^{-1}), good restoration capability (~ 91%), and excellent cycling stability (~ 88% retention after 250 cycles) with a coulombic efficiency of 99%, revealing its outstanding potentiality for high–performance LIBs. Our experimental findings and analysis demonstrated the direct hydrothermal synthesis of binder–free CCO anode materials to maximize the LIB performance via the control of the self-assembling growth using various solvent media with different viscosity.

Results and Discussion

The crystal phase formation of the $CuCo_2O_4$ were analysed by X–ray diffractometry (XRD) measurements, as shown in Figure 2a. The diffraction peaks observed at 19.18°, 31.33°, 36.88°, 38.62°, 44.85°, 55.71°, 59.37°, and 65.63° correspond to the diffraction from the (111), (220), (311), (222), (400), (422), (511) and (440) planes, respectively. These diffraction peaks revealed the polycrystalline nature of the $CuCo_2O_4$ and could be assigned to its cubic structure (JCPDS card no. 01–1155). The almost identical XRD spectra among the various products suggested that the different solvents used for the synthesis did not affect the crystallinity and crystal phase of $CuCo_2O_4$, however they may modify their surface morphology. The absence of other noticeable planes confirmed the phase purity of $CuCo_2O_4$. This was further supported by the Raman spectra. Figure 2b shows the Raman spectra of the $CuCo_2O_4$, which revealed a wide peak that was deconvoluted into three peaks centered at 648, 543, and 470 cm^{-1} and corresponding, respectively, to the A_{1g}, F_{2g}, and E_g vibrational modes of $CuCo_2O_4$.[34]

Moreover, energy dispersive spectroscopy (EDS) was performed to determine the chemical composition of the samples (Figure S1, Supplimentary Information). The histogram extracted from EDS spectra (Figure 2c) revealed that the constituting elements (i.e., Cu, Co, and O) were stoichiometrically present in the various films with almost identical composition ratios, regardless of the solvent used.

The full–range X–ray photoelectron spectroscopy (XPS) survey results for the various $CuCo_2O_4$ films (Figure 3a) further confirmed the presence of Co, Cu, and O. The observed XPS peaks were modelled via Gaussian curve fitting. The Co 2p spectra (Figure 3b) showed two main emission peaks at 779.65 and 794.85 eV corresponding to Co $2p_{3/2}$ and Co $2p_{1/2}$, respectively, and with a spin–energy separation of 15.0 eV that indicate the presence of cobalt in the Co^{3+} oxidation state.[35] The Cu 2p spectra (Figure 3c) were well fitted into a spin–orbit doublet centred at 933.70 eV and a satellite peak at 942.05 eV was also observed, revealing the Cu^{2+} oxidation state. The O 1s spectra (Figure 3d) were deconvoluted into three peaks designated as O_1, O_2, and O_3, corresponding, respectively, to the metal–oxygen bonds, non–stoichiometric oxygen coordination, and multiplicity of chemi–sorbed and physi–sorbed water at or near the surface.[35,36.] The observed oxidation states of Co^{3+}, Cu^{2+} and O^{2-} confirmed the formation of the $CuCo_2O_4$.

Figure 4 shows the field–emission scanning electron microscopy (FE–SEM) images of the various $CuCo_2O_4$ films. Each sample exhibited a unique morphology according to the solvent used; the organic solvents had different polarity and viscosity, affecting the reaction speed that plays a crucial role in determining the surface morphology. The $CuCo_2O_4$ film synthesized using deionized water (DIW) as a solvent (CCO_{DIW}) showed a porous nanosheet morphology with a thickness below 30 nm (Figure 4a). The film obtained with etanol (E) as solvent (CCO_E) exhibited a cubic–like structures with an average size of ~350 nm (Figure 4b); each cubic structure consisted of many smaller grains. In the case of ethylene glycol (EG) as a solvent (CCO_{EG}), a compact granular morphology was observed (Figure 4c). The one synthesised with glycerol (G; CCO_G) showed numerous agglomerated spherical particles having different diameters (Figure 4d). These morphological differences were attributed to divergent growth mechanisms during the hydrothermal process associated with the different solvents, whose viscosity determined the growth rate of the active materials, changing the way of nucleation and, hence, resulting in different morphologies.

The microscopic structural properties of the CCO_{DIW} film were investigated using various techniques, including (Figure 5) bright–field transmission electron microscopy (BFTEM), high–resolution TEM (HRTEM), selected–area electron diffraction (SAED), EDS scanning TEM (EDS–STEM) line mapping, and elemental mapping. The BFTEM image of a nanosheet from the CCO_{DIW} sample is shown in Figure 5a; contained many nanopores (white space) on the surface were also observed by SEM (Figure 4a). The HRTEM image (Figure 5b) showed randomly oriented lattice fringes, confirming the polycrystalline nature of the $CuCo_2O_4$ film; the indexed interplanar distance (inset) corresponds to the d–spacing of the cubic $CuCo_2O_4$ {311} lattice plane. Moreover, the discontinuous SAED ring patterns (Figure 5c) embedded within large spots were indexed to {400}, {111}, and {220} reflections, further confirming the cubic crystal configuration and polycrystalline nature of the CCO_{DIW} film.[37,38] At the atomic scale, the elemental distribution of Cu, Co, and O across the nanosheet was obtained via EDS–

STEM line mapping (Figure 5d), which showed the homogeneous existence of these elements. The EDS–STEM chemical mapping images (Figures 5e–h) of the CCO_{DIW} sample, further assessed their uniform distribution throughout the nanosheet.

The effective surface areas and pore size distributions of the various $CuCo_2O_4$ films, which are crucial in determining the Li^+ storage capacity and transport, could be evaluated using, respectively, Brunauer–Emmett–Teller (BET) method and the Barrett–Joyner–Halenda (BJH) method based on N_2 liguid state adsorption–desorption isotherms recorded at 77 K (Figures 6a,b). CCO_{DIW} exhibited the largest BET specific surface area ($a_{s–BET}$, of 90.65 m^2 g^{-1}) compared to CCO_E (60.39 m^2 g^{-1}), CCO_{EG} (37.65 m^2 g^{-1}), and CCO_G (34.21 m^2 g^{-1}); this larger value might be ascribed to the unique two-dimensional (2D) nanosheet morphology with a porous architecture on the CCO_{DIW} surface and may result in more channels and locations, which is favorable for the rapid intercalation/de–intercalation of Li^+ ions during the charging and discharging processes. Figure 6c shows the corresponding BJH plots calculated from the measured N_2 isotherm curves for the $CuCo_2O_4$ samples, revealing that the pore size distribution ranged between the mesopore and micropore regions; CCO_{DIW} exhibited average BJH pore diameter and volume of 15.53 nm and 0.33 cm^3 g^{-1}, respectively, which are larger values compared to CCO_E (13.60 nm and 0.23 cm^3 g^{-1}), CCO_{EG} (10.90 nm and 0.15 cm^3 g^{-1}), and CCO_G (9.24 nm and 0.10 cm^3 g^{-1}). This large pore volume could ease the Li^+ diffusion and extraction into and out of the active material with a small resistance and even buffer its volume expansion during charging and discharging processes. Thus, since the CCO_{DIW} sample exhibited higher $a_{s–BET}$, larger pore diameter and pore volume, a better electrochemical anode performance was expected when using it in LIBs.

The electrochemical performance of the various $CuCo_2O_4$ films as LIB anodes was systematically studied via cyclic votammetry (CV), discharge–charge, and electrochemical impedance spectroscopy (EIS). Figure 7 shows the initial five CV curves between 0.005 and 3.0 V *vs* Li/Li$^+$ for the various $CuCo_2O_4$ anodes, at a scan rate of 0.1 mV s^{-1}, while the scan rate–dependent CV curves are presented in Figure S2 (Supplementary Information). The possible electrochemical reactions can be summarized as follows.[26,29,36]

$$CuCo_2O_4 + 8\,Li^+ + 8e^- \rightarrow Cu + 2\,Co + 4\,Li_2O \tag{1}$$

$$Cu + Li_2O \leftrightarrow CuO + 2\,Li^+ + 2\,e^- \tag{2}$$

$$2\,Co + 2\,Li_2O \leftrightarrow 2\,CoO + 4\,Li^+ + 4\,e^- \tag{3}$$

$$2\,CoO + 2/3\,Li_2O \leftrightarrow 2/3\,Co_3O_4 + 4/3\,Li^+ + 4/3\,e^- \tag{4}$$

In the first cathodic sweep, three reduction peaks were observed. The well–defined and intense reduction peak at ~ 0.58 V *vs* Li/Li$^+$ could be assigned to a solid electrolyte interface (SEI) layer formation, caused by electrolyte decomposition during the first discharge.[28,29] The less intense peak at ~ 0.84 V was attributed to the reduction of Cu^{2+} and Co^{2+} to metallic Cu and Co (with similar reduction potentials), respectively, in an amorphous Li_2O matrix.[39,40] The weak peak at ~ 1.2 V *vs* Li/Li$^+$ was due to the reduction of Co^{3+} to Co^{2+}. In the subsequent CV cycles, the abovementioned cathodic peak at ~ 0.58 V *vs* Li/Li$^+$ disappeared because of the irreversible faradaic electrochemical reaction associated with the SEI layer formation on the electrode surface during the first discharge cycle, while the other other two peaks shifted toward higher potential values (one from ~ 0.84 to ~ 1.0 V and the other from ~ 1.2 V to ~ 1.29 V.[29–31] In the corresponding anodic sweep, two broad oxidation peaks (down arrows) were observed at ~ 1.45 and ~ 2.20 V and could be assigned to the oxidation of metallic Cu and Co to, respectively, CuO and CoO → Co_3O_4.[41–45] No obvious change was observed in the position and intensity of the peaks from the second cycle, indicating good electrochemical reversibility during the successive cycles.

Figure 8 shows the initial five discharge–charge GCD curves for the various $CuCo_2O_4$ anodes at 0.1 A g^{-1}; the voltage plateaus (around 1.20 and 0.84 V during the discharge and around ~ 1.45 and ~ 2.20 V during the charge) were associated with the reduction–oxidation peaks observed in the CV curves and consistent with their results. The CCO_{DIW} anode clearly exhibited the largest discharge capacity compared with the other $CuCo_2O_4$ anodes. The first specific discharge capacities for the $CCO_{DIW,}$ CCO_E, CCO_{EG}, and CCO_G anodes were 1547, 1176, 905, and 718 mAh g^{-1}, respectively and these values were reduced to 1172, 883, 600, and 425 mAh g^{-1} in the following cycles. This decreasing trend was associated with the SEI layer formation and the values remained almost unchanged in the next succeeding cycles, revealing excellent cycle stability and electrochemical robustness.

Figure 9a shows the rate capability of the various $CuCo_2O_4$ anodes at different current densities (0.1–5 A g^{-1}). As the current density increases the specific charge/discharge capacity decreases nonlinearly because of non–linear behaviour of the Li^+ diffusion at the electrode–electrolyte interface. At 0.1 A g^{-1}, CCO_{DIW} (with a nanosheet morphology) reached the highest specific charge and discharge capacities (respectively, 1820 mAh g^{-1} and 1547 mAh g^{-1}) compared with the other anodes; at a very high current density (5 A g^{-1}), it still exhibited superior specific charge and discharge capacities (respectively, 720 and 789 mAh g^{-1}). When the current density returns to 0.1 A g^{-1}, the restoration capability of the $CuCo_2O_4$ anodes were 91 % for CCO_{DIW}, 79 % for CCO_E, 88 % for CCO_{EG}, and 83% for CCO_G.

The charge–discharge stability of the $CuCo_2O_4$ anodes was tested and compared at a high current rate (1 A g^{-1}, Figure 9b). Their specific capacity decreased slowly (e.g., for the CCO_{DIW} anode, from 954 to 749 mAh g^{-1} after 130 cycles) due to capacity fading but, then, it recovered (from 749 to 837 mAh g^{-1} after 250 cycles), presumably because of the electrochemical activation of the active materials after the reversible growth of a polymeric gel–like film;[46–49] this trend was observed for all the anodes. The CCO_{DIW}, CCO_E, CCO_{EG}, and CCO_G anodes attained capacity retentions of about 88, 71, 63 and 60% and coulombic efficiencies of about 99, 94, 91 and 90%, respectively, after 250 discharge–charge cycles. These decrease in specific capacity was due to a slightly improved charge–transfer resistance. Moreover, the CCO_{DIW} anode exhibited good sustainability when tested at both low and high current rates (0.2, 1.0 and 5.0 A g^{-1}) over 250 discharge–charge cycles (Figure 9c); its superior capacity endurance compared with the others CCO anodes, was probably related to the synergetic effect of porous architecture and structural integrity of its 2D nanosheets grown on its current collector.

The excellent battery performance of the synthesized CCO anodes was clarified by understanding their electrochemical reaction kinetics via the scan rate–dependent CV measurements; the intergrated area under the CV curves was a measure of the stored charge amount that arising from surface or interface capacitive–controlled process and the semi–infinite linear diffusion process. The reaction kinetics–based diffusive and capacitive current response at different scan rates was characterised via a quantitative CV analysis. The current response (i) obeys the following power–law:[50,51]

$$i = \mathrm{a} \cdot v^{b}, \tag{5}$$

where a is an adjustable fitting parameter, b is the slope of the log (i) vs. log (v) plot, while i and v (scan rate) values were extracted from the experimental data and are presented in Figure S2 (Supplementary Information). Figure 10a shows the b–value (extracted from Figure S3, Supplementary Information), which ranged between 0.5 (diffusion–controlled) and 1.0 (surface capacitive–controlled).[52] At 0.5 V in the cathodic region, a value of 1.0 revealed that the interface capacitive–controlled process was dominant. When the cathodic potential increased to 1.0 V, the *b*–value dropped to 0.5, suggesting that the current response was dominated only by the Li^+ diffusion process. As the potential increased further to 2.0 V, the *b*–value increased up to ~ 0.71, demonstrating that the current response was driven by both the surface capacitance and the Li^+ intercalation mechanism. Afterwards, decreased again, forming a peak at 2.0 V and revealing a sensitive change in the charge storage mechanism of the active materials with the potential.

To quantitatively separate the response current into surface–capacitive ($k_1 \times v$) and intercalation ($k_2 \times v^{1/2}$) contributions at a fixed potential, the following equation can be used:[53,54]

$$i(v)/v^{1/2} = k_1 \times v^{1/2} + k_2 \,, \tag{6}$$

where k_1 and k_2 are fitting parameters and their values are presented in Figure S4 (Supplementary Information). Figure 10b shows the relative capacitive and intercalation contributions for the $CuCo_2O_4$ anodes at different scan rates; this electrochemical kinetic analysis revealed that the Li^+ intercalation contribution was non–linearly suppressed by increasing the scan rate. Figures 10c,d show the surface–capacitive (shaded region) and intercalation (unshaded space) contributions under the CV curves at 0.1 and 5 mV s^{-1}, respectively, for the CCO_{DIW} anode; similar CV analysis plots for the CCO_E, CCO_{EG}, and CCO_G anodes are presented in Figure S5 (Supplementary Information). The CCO_{DIW} anode clearly exhibited better Li^+ storage property, as evidenced from the strong current response in the CV curves (Figure 7), and higher discharge capacity (Figure 8) compared with the other $CuCo_2O_4$ anodes. These CV and battery performance results could be further understood via the systematic analysis of Eq. (6) (Figure 10b); the enhanced Li^+ storage capacity of the

CCO_{DIW} anode was mainly due to its surface morphology, favorable for the Li^+ transport and storage at the electrode–electrolyte interface.

The kinetics of the electron transfer reactions for the CCO anodes were investigated via EIS measurements. Figure 11a shows the Nyquist plots of all of them. This plot type consists of a straight line and a semicircle in the low– and high–frequency regions, respectively; the former (Warburg impedance: W_0) is associated with the faradaic redox and the latter with the charge transfer resistance (R_{ct}).[55,56] The intersection of the semicircle at the x-axis represents the internal resistance of the anodes (R_S). The mesoporous CCO_{DIW} nanosheet anode exhibited the smallest semicircle, corresponding to the smallest R_{ct}. The Nyquist plots before and after the discharge/charge stability tests and the extracted parameter values are presented, respectively, in Figure S6 and Table S2 (Supplementary Information). As anticipated, the CCO_{DIW} anode exhibited much lower R_{ct} (3.26 Ω) and R_{SEI} (resistance due to SEI layer formation: 2.31 Ω) values compared to the CCO_E (7.33 and 3.59 Ω), CCO_{EG} (24.23 and 11.92 Ω), and CCO_G (42.11 and 13.83 Ω) ones. Thus, its superior performance was associated with the inherent excellent ionic and electronic conductivities at the electrode–electrolyte and electrode–current collector interfaces.

Charge transfer resistance and morphology–dependent $a_{S\text{-}BET}$ are key factors determining the specific capacity, and hence, possible relationships between them can be naturally expected. Figure 11c shows $a_{s\text{–}BET}$, R_{ct} and the specific capacity as functions of the solvent viscosity. As the solvent viscosity increased, noticeable and consistent trends were observed; as expected, $a_{S\text{-}BET}$ increased, while R_{ct} exhibited the opposing behaviour. Since the growth rate was considerably influenced by the solvent viscosity, the associated morphology change generated different environments for the charge storage reactions.

Conclusions

We fabricated binder–free $CuCo_2O_4$–based anodes on Ni foam current collectors via a mild single–step hydrothermal growth technique. The surface morphology of the $CuCo_2O_4$ active material was tuned from nanosheet to cubic, granular, and agglomerated spheres by simply changing the solvents used, i.e., de–ionised water, ethanol, ethylene glycol, and glycerol. All the $CuCo_2O_4$ films exhibited very similar chemical composition, structural phase, and crystallinity, but different surface morphology. The mesoporous $CuCo_2O_4$ anode, which had a nanosheet morphology, reached a maximum specific capacity of 1547 mAh g^{-1} at 0.1 A g^{-1}, with superior restoration performance. The LIB performance of all these $CuCo_2O_4$ anodes was strongly dependent on the surface morphology since this influenced their charge transfer kinetics and Li^+ storage capability.

Experimental Section

Preparation of the Anode Films: The analytical grade purity chemicals, purchased from Sigma Aldrich, were used as received. The $CuCo_2O_4$ films were directly grown on Ni foam substrates via a one–pot mild hydrothermal route (Figure 12). In a typical synthesis, $CoCl_2 \cdot 6H_2O$ (6 mmol) and $CuCl_2 \cdot 2H_2O$ (3 mmol) were dissolved in DIW (40 ml) followed by the addition of CH_4N_2O (urea, 18 mmol) under vigorous stirring at room temperature until the mixture solution turned into transparent–pink color. After 30 min, both the pre–cleaned Ni foam substrate (Figure 12a) and the mixture solution were transferred into a 100 ml Teflon–lined stainless–steel autoclave, kept in a muffle furnace, and heated at 120 °C for 6 h (Figure 12b). After natural cooling to room temperature, the film samples (green color in Figure 12b) were washed with E and DIW, dried at room temperature overnight and, then, calcined at 300 °C for 2 h in air ambient with a ramping rate of 1 °C min^{-1} in a tubular furnace. All the growth parameters except for the solvent used, were kept constant for each CCO sample.

Material Characterisation: The crystallinity and phase confirmation of the $CuCo_2O_4$ films were examined with an X–ray diffractometer using CuK_α radiation (λ = 1.54056 Å; Rigaku Smartlab) with a scanning rate of 2° min^{-1} in the 20°–80° 2θ range, at 40 kV and 30 mA. Their Raman spectra were obtained using a spectrometer (LabRam Armis; Horiba Jobin Yvon) and an Ar–ion laser beam (λ = 514.5 nm). The morphological structure and elemental composition of the $CuCo_2O_4$ films were characterised via FE–SEM and EDS; the EDS spectra were obtained at a 5000x magnification with a JSM–6701F microscope (Japan) operating at 15 kV. The binding energy of the constituents elements was determined through XPS measurements on a PHI 5000 VersaProbe spectrometer (ULVAC PHI, Japan); their oxidation states were calibrated by the C 1s position (284.8 eV) of the carbon contaminant inside the vacuum chamber of the XPS instrument. The SAED patterns, TEM (JEOL–3000F; Oxford Instrument) images, and HR–TEM images along with the elemental mapping were obtained at 300 kV.

Electrochemical LIB Measurements: The electrochemical properties of the $CuCo_2O_4$ anode films were investigated using coin–type cells (CR2032) on a battery cycler (Bio–Logic Scientific Instruments, France); the test cells were fabricated in an argon–filled glove box (Kyon, Korea). A $CuCo_2O_4$ electrode film (15 mm disc) and a lithium metal foil were used as the working and counter electrodes, respectively, separated by a separator (Celgard 2400). An electrolyte of 1 M $LiPF_6$ solution was used, which is a mixed solvent (50:50, v/v) of ethyl carbonate (EC) and diethylene carbonate (DEC). The electrochemical behaviours of the $CuCo_2O_4$ anodes were investigated by CV, discharge–charge, and EIS measurements. The CV analysis was performed at different scan rates (0.1–5 mV s^{-1}) in a potential window range between 0.005 and 3.0 V (vs. Li/Li$^+$). The fabricated cells were discharged–charged at different current densities (0.1 and 5 A g^{-1}). The EIS was conducted to help understand the charge–transfer kinetics in a frequency range between 1 and 10 kHz.

Supporting Information

Supporting Information is available from the Wiley Online Library or from the author.

It reports the scan rate–dependent CV curves at different scan rates, the log (*i*) vs. log (*v*) plots for the *b*–value estimation and relative capacitive and diffusive contribution ratio analysis for all the fabricated $CuCo_2O_4$ anodes, performed using Eq. (6). It also includes the interface and surface capacitive contribution, at 0.1 and 5.0 mV s^{-1}, for the CCO_E, CCO_{EG}, and CCO_G anodes.

Acknowledgments

The authors would like to thank the financial support from the National Research Foundation (NRF) of Korea (Grant nos. 2015M2A2A6A02045251, 2018R1A2B6007436, 2016R1A6A1A03012877, and 2015R1D1A1A01060743).

Received: ((will be filled in by the editorial staff))
Revised: ((will be filled in by the editorial staff))
Published online: ((will be filled in by the editorial staff))

References

[1] Y. Yin, W. Liu, N. Huo, and S.Yang, *Chemical Engineering Journal*, **2017**, *307*, 999.

[2] A. I. Inamdar, H..S. Chavan, A. T. A. Ahmed, S. Cho, J. Kim, Y. Jo, S. M. Pawar, Y. Park, H. Kim, H. Im, *Materials Letters*, **2018**, *215*, 233.

[3] Y. Wu, J. Meng, Q. Li, C. Niu, X. Wang, W. Yang, W. Li, and L. Mai, *Nano Research*, **2017**, *10*, 2364.

[4] J. E. Lee, S. H. Yu, D. J. Lee, D. C. Lee, S. I. Han, Y. E. Sung and T. Hyeon, *Energy Environ. Sci.*, **2012**, *5*, 9528.

[5] J. M. Tarascon, and M. Armand, *Nature*, **2001**, *414*, 359.

[6] B. Wang, X. Li, X. Zhang, B. Luo, M. Jin, M. Liang, S. A. Dayeh, S. T. Picraux, and L. Zhi, *ACS Nano*, **2013**, *7*, 1437.

[7] R. Dash, and S. Pannala, *Scientific report*, DOI: 10.1038/srep27449.

[8] Z. Xiong, Y. S. Yun, and H. J. Jin, *Materials*, **2013**, *6*, 1138.

[9] F. D. Wu, and Y. Wang, *J. Mater. Chem.*, **2011**, *21*, 6636.

[10] M. Reddy, T. Yu, C. H. Sow, Z. X. Shen, C. T. Lim, G. Subba Rao, and B. Chowdari, *Adv. Funct. Mater.*, **2007**, *17*, 2792.

[11] B. Wang, J. S. Chen, H. B. Wu, Z. Wang, and X. W. Lou, *J. Am. Chem. Soc.*, **2011**, *133*, 17146.

[12] M. Chena, J. Li, D. Chao, J. Wang, J. Yin, J. Lin, H. J. Fan, and Z. X. Shen, *Nano Energy*, **2014**, *9*, 364.

[13] N. Yan, X. Zhou, Y. Li, F. Wang, H. Zhong, H. Wang, and Q. Chen, *Scientific Report*, **2013**, *3*, 3392.

[14] J. X. Zhu, Z. Y. Yin, D. Yang, T. Sun, H. Yu, H. E. Hoster, H. H. Hng, H. Zhang, and Q. Y. Yan, *Energy Environ. Sci.*, **2013**, *6*, 987.

[15] H. S. Jadhav, G. M. Thorat, J. Mun, J. G. Seo, *Journal of Power Sources*, **2016**, *302*, 13.

[16] H. T. Sun, G. Q. Xin, T. Hu, M. P. Yu, D. L. Shao, X. Sun, and J. Lian, *Nat. Commun.*, **2014**, *5*, 4526.

[17] H. S. Jadhav, A. K. Rai, J. Y. Lee, J. Kim, and C. J. Park, *Electrochimica Acta*, **2014**, *146*, 270.

[18] Y. Li, B. Tan, and Y. Wu, *Nano Lett.*, **2008**, *8*, 265.

[19] Y. Sun, X. Hu, W. Luo, and Y. Huang, *J. Phys. Chem. C*, **2012**, *116*, 20794.

[20] C. Peng, B. Chen, Y. Qin, S. Yang, C. Li, Y. Zuo, S. Liu, and J. Yang, *ACS Nano*, **2012**, *6*, 1074.

[21] J. C. Park, J. Kim, H. Kwon, and H. Song, *Adv. Mater.*, **2009**, *21*, 803.

[22] M. V. Reddy, C. Yu, F. Jiahuan, K. P. Loh, and B. V. R. Chowdari, *ACS Appl. Mater. Interfaces*, **2013**, *5*, 4361.

[23] J. Zhang, B. Wang, J. Zhou, R. Xia, Y. Chu, and J. Huang, *Matrrials*, **2017**, *10*, 72.

[24] Y. T. Xu, Y. Guo, C. Li, X. Y. Zhou, M. C. Tucker, X. Z. Fu, R. Sun, and C. P. Wong, *Nano Energy*, **2015**, *11*, 38.

[25] J. Ma, H. Wang, X. Yang, Y. Chai, and R. Yuan, *J. Mater. Chem. A*, **2015**, *3*, 12038. PCC-CCO

[26] S. M. Pawar, B. S. Pawar, B. Hou, A. T. A. Ahmed, H. S. Chavan, Y. Jo, S. Cho, J. Kim, J. Seo, S. N. Cha, A. I. Inamdar, H. Kim, H. Im, *Journal of Industrial and Engineering Chemistry*, **2019**, *69*, 13.CCO NS

[27] J. Cheng, X. Lin, Z. Wang, H. Guo, W. Peng, and Q. Hu, *Ceramics International*, **2016**, *42*, 2871. FNC CCO

[28] H. Zhang, Z. Tang, K. Zhang, L. Wang, H. Shi, G. Zhang, H. Duan, *Electrochimica Acta*, **2017**, *247*, 692. CCO/C NF

[29] F. Jiang, Q. Su, H. Li, L. Yao, H. Deng, and G. Du, *Chemical Engineering Journal*, **2017**, *314*, 301. CCO/G

[30] S. Cai, G. Wang, M. Jiang, and H. Wang, *J. Solid State Electrochem*, **2017**, *21*, 1129. PHS CCO

[31] F. Niu, N. Wang, J. Yue, L. Chen, J. Yang, Y. Qian, *Electrochimica Acta*, **2016**, *208*, 148. PMFs CCO

[32] M. Li, Y. X. Yin, C. Li, F. Zhang, L. J. Wan, S. Xu, and D. G. Evansa, *Chem. Commun.*, **2012**, *48*, 410.

[33] G. Zhang, X. W. Lou, *Adv. Mater*. **2013**, *25*, 976.

[34] J. Cheng, H. Yan, Y. Lu, K. Qiu, X. Hou, J. Xu, L. Han, X. Liu, J. K. Kime, Y. Luo, *J. Mater. Chem. A*, **2015**, *3*, 9769.

[35] L. Han, T. Yu, W. Lei, W. Liu, K. Feng, Y. Ding, G. Jiang, P. Xu, and Z. Chen, *J. Mater. Chem. A*, **2017**, 5, 16568.

[36] H. S. Jadhav, S. M. Pawar, A. H. Jadhav, G. M. Thorat, and J. G. Seo, *Scientific reports*, **2016**, *6*, 31120.

[37] N. Kattana, B. Houb, D. J. Fermínb, and D. Cherns, *Applied Materials Today*, **2015**, *1*, 52.

[38] B. Hou, D. B. Alifonso, N. Kattan, D. Cherns, M. C. Galan, and D. J. Fermn, *Chem. Eur. J.* **2013**, *19*, 15847.

[39] M. Bhardwaj, A. Suryawanshi, R. Fernandes, S. Tonda, A. Banerjee, D. Kothari, S. Ogale, *Materials Research Bulletin*, **2017**, *90*, 303.

[40] H. S. Jadhav, S. M. Pawar, A. H. Jadhav, G. M. Thorat, and J. G. Seo1, *Scientific Reports*, **2016**, *6*, 31120.

[41] B. Qu, *ACS Appl. Mater. Interfaces*, **2014**, *6*, 731.

[42] Y. Sharma, N.Sharma, G. V. S.Rao, and B. V. R.Chowdari, J. Power Sources, **2007**, *173*, 495.

[43] P. Poizot, S. Laruelle, S. Grugeon, L. Dupont, J. M. Tarascon, *Nature* **2000**, *407*, 496.

[44] X. P. Gao, J.L. Bao, G.L. Pan, H.Y. Zhu, P.X. Huang, F. Wu, D.Y. Song, *J. Phy. Chem. B*, **2004**, *108*, 5547.

[45] Y. Sharma, N. Sharma, G. V. Subba Rao, B. V. R. ChowdarI, *Adv. Funct. Mater.*, **2007**, *17*, 2855.X

[46] A. Ponrouch, P. L. Taberna, P. Simon, M.R. Palacín, *Electrochim. Acta*, **2012**, *61*, 13.

[47] Z. Xu, Y. Liu, W.X. Zhao, B. J. Li, X. Zhou, H. Shen, *Electrochimica Acta*, **2016**, *190*, 894.

[48] E. M. Lotfabad, P. Kalisvaart, A. Kohandehghan, D. Karpuzov, D. Mitlin, *J. Mater. Chem. A*, **2014**, *2*, 19685.

[49] J. Yue, X. Gu, L. Chen, N.N. Wang, X.L. Jiang, H.Y. Xu, J. Yang, Y.T. Qian, *J. Mater. Chem. A*, **2014**, *2*, 17421.

[50] J. Wang, J. Polleux, J. Lim, and B. Dunn, *J. Phys. Chem. C*, **2007,** *111,* 14925.

[51] S. Lou, X. Cheng, Y. Zhao, A. Lushington, J. Gao, Q. Li, P. Zuo, B. Wang, Y. Gao, Y. Ma, C. Du, G. Yin, X. Sun, *Nano Energy*, **2017**, *34*, 15.

[52] M. R. Lukatskaya, B. Dunn, and Y. Gogotsi, *Nat. comm.*, **2016**, *7*, 12647.

[53] K. Zhao, F. Liu, C. Niu, W. Xu, Y. Dong, L. Zhang, S. Xie, M. Yan, Q. Wei, D. Dhao, and L. Mai, *Adv. Sci.* **2015**, *2*, 1500154.

[54] D. Chao, C. Zhu, P. Yang, X. Xia, J. Liu, J. Wang, X. Fan, S. V. Savilov, J. Lin, H. J. Fan, and Z. X. Shen, *Nat. comm.*, **2016**, *7*, 12122.

[55] M. Guo, J. Balamurugan, T. D. Thanh, N. H. Kim, J. H. Lee, *J. Mater. Chem. A*, **2016**, *4*, 17560.

[56] L. Qian, L. Gu, L. Yang, H. Yuan, and D. Xiao, *Nanoscale*, **2013**, *5*, 7388.

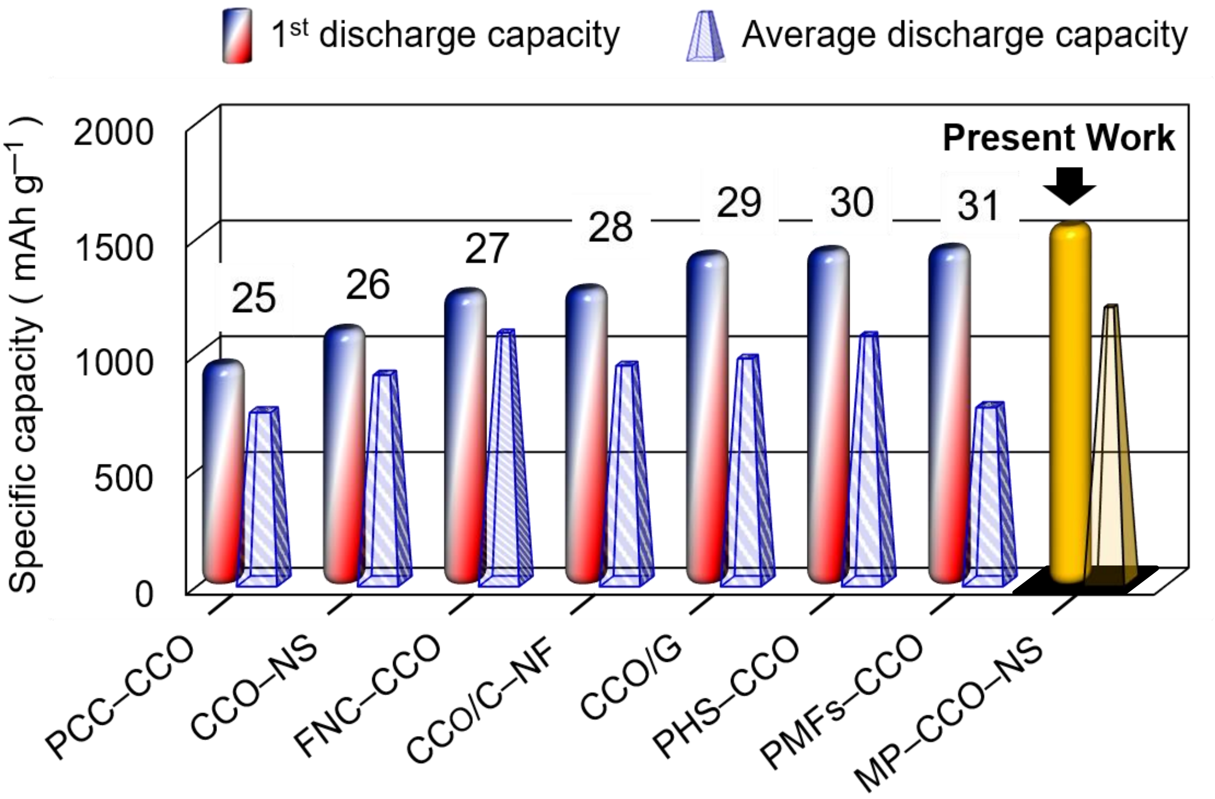

Figure 1. Comparison of the specific capacity of $CuCo_2O_4$ (CCO) LIB anodes measured in the present work and in previous studies (PCC: porous carbon–coated; NS: nanosheets; FNC: FeO nanowires–connected; C–NF: carbon composite nanofiber; G: graphene; PHS: porous hollow sphere; PMFs: porous microflowers; MP: mesoporous).

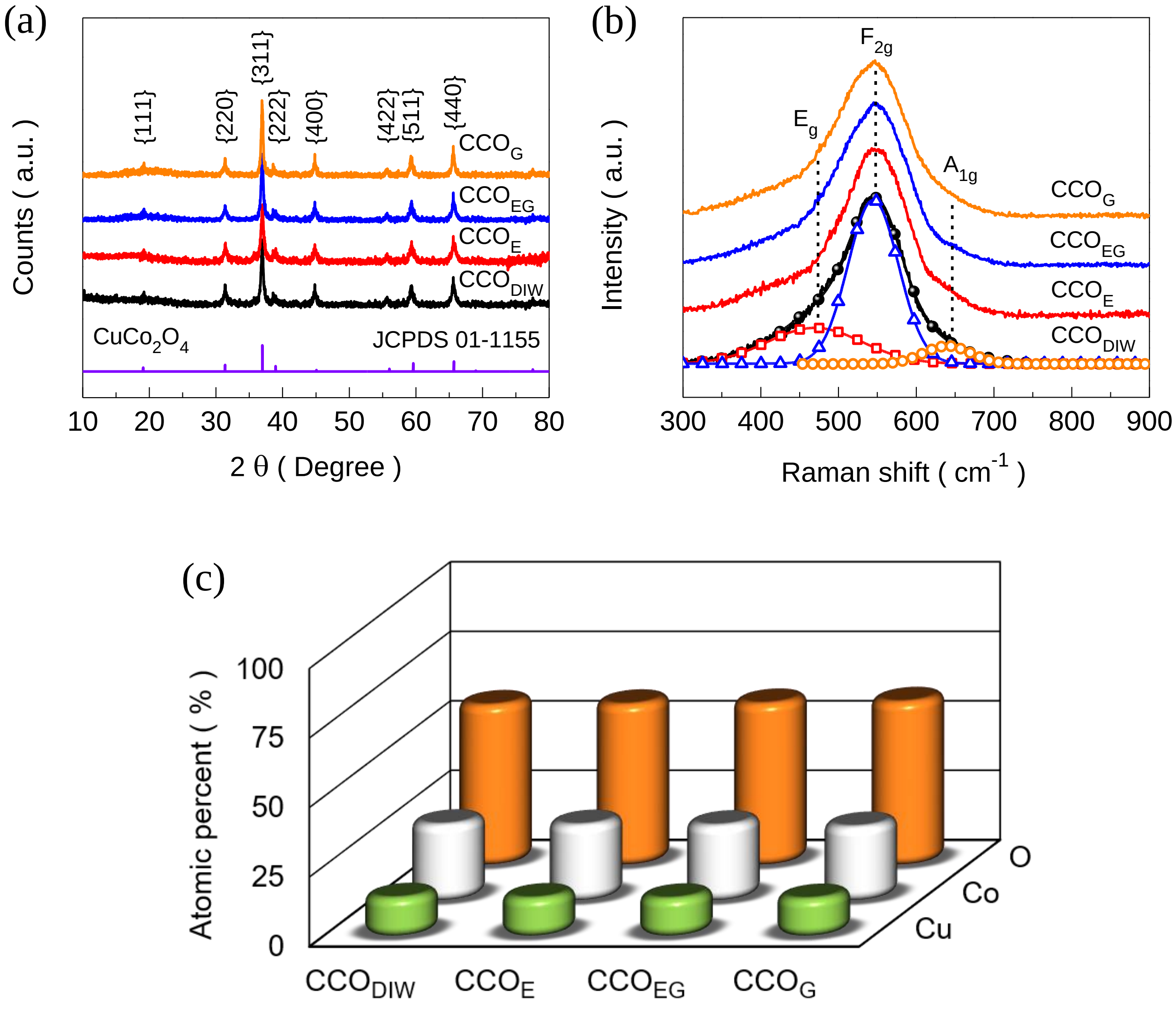

Figure 2. (a) X–ray diffraction (XRD), (b) Raman spectra, and (c) energy dispersive spectroscopy (EDS) histogram of the CuCo$_2$O$_4$ films synthesized via a hydrothermal procedure under the influence of solvents, namely, deionized water (DIW), eyhanol (E), ethylene glycol (EG), and glycerol (G). The evident similarities among them revealed that the underlying

crystallinity, structural phase, and chemical compositions of the $CuCo_2O_4$ films were does not affected by the solvent variation.

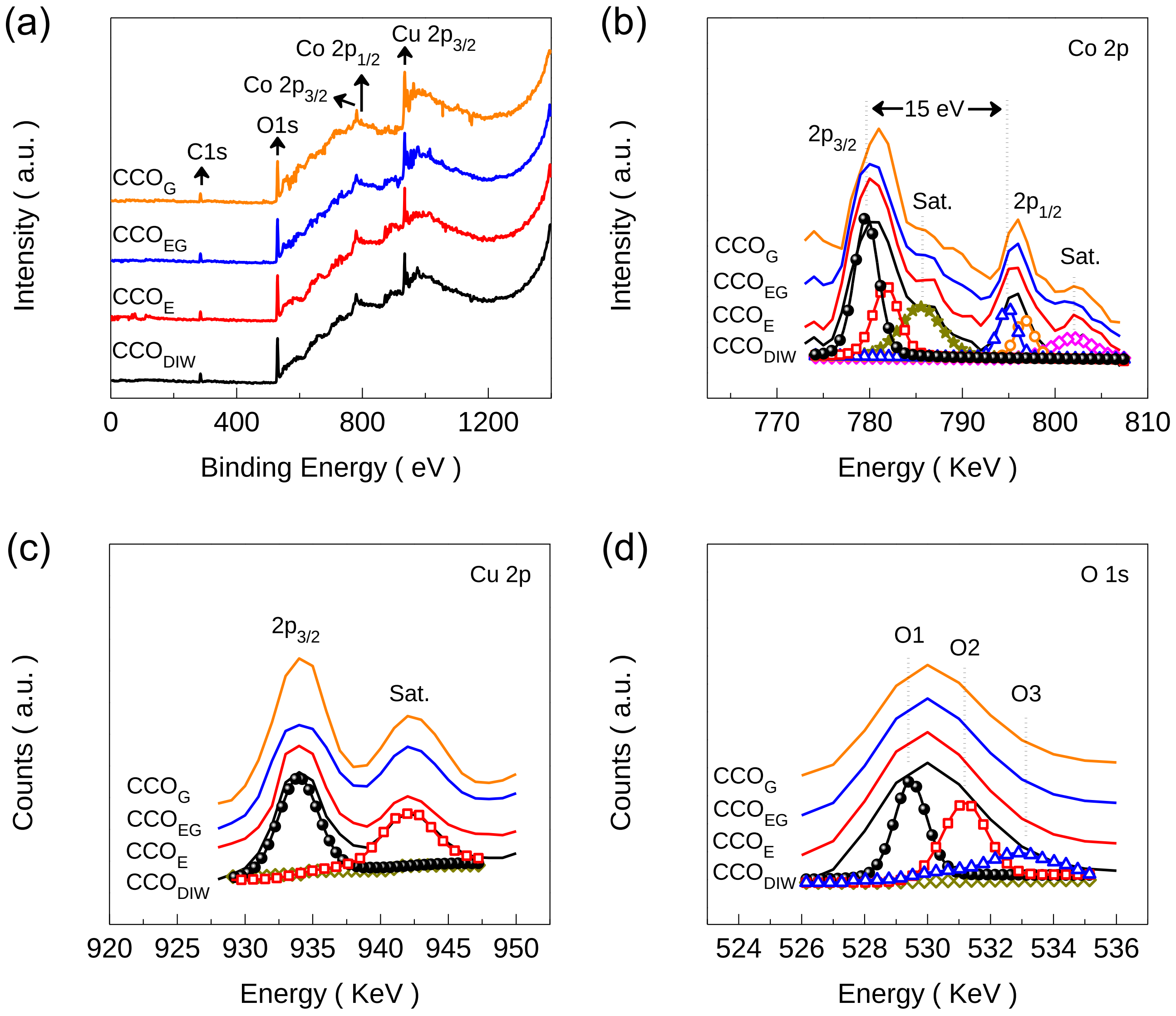

Figure 3. (a) Full–range X–ray photoelectron survey, (b) Co 2p, (c) Cu 2p, and (d) O1s of the $CuCo_2O_4$ films prepared by various solvents. The single–element spectra were deconvoluted by the Gaussian curve fitting model (Sat.: satellite peak).

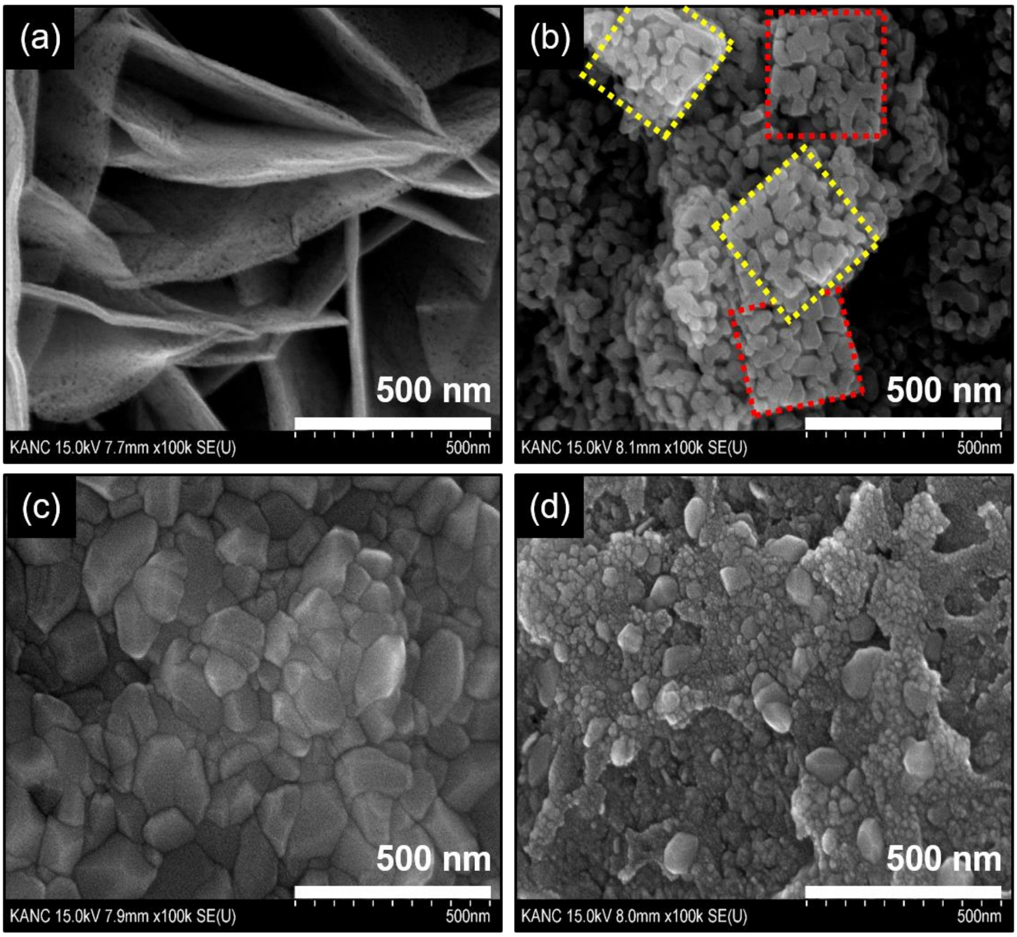

Figure 4. (a) Field–emission scanning electrom microscopy images of the $CuCo_2O_4$ (CCO) films, synthesized with various solvents (DIW: deionized water; E: ethanol; EG: ethylene

glycol; G: glycerol), showing different morphologies: (a) mesoporous nanosheet morphology for CCO_{DIW}, (b) cubic morphology for CCO_{E}, (c) granular morphology for CCO_{EG}, and (d) agglomerated embossing morphology for CCO_{G}. An enlarged view of each image is shown in the inset.

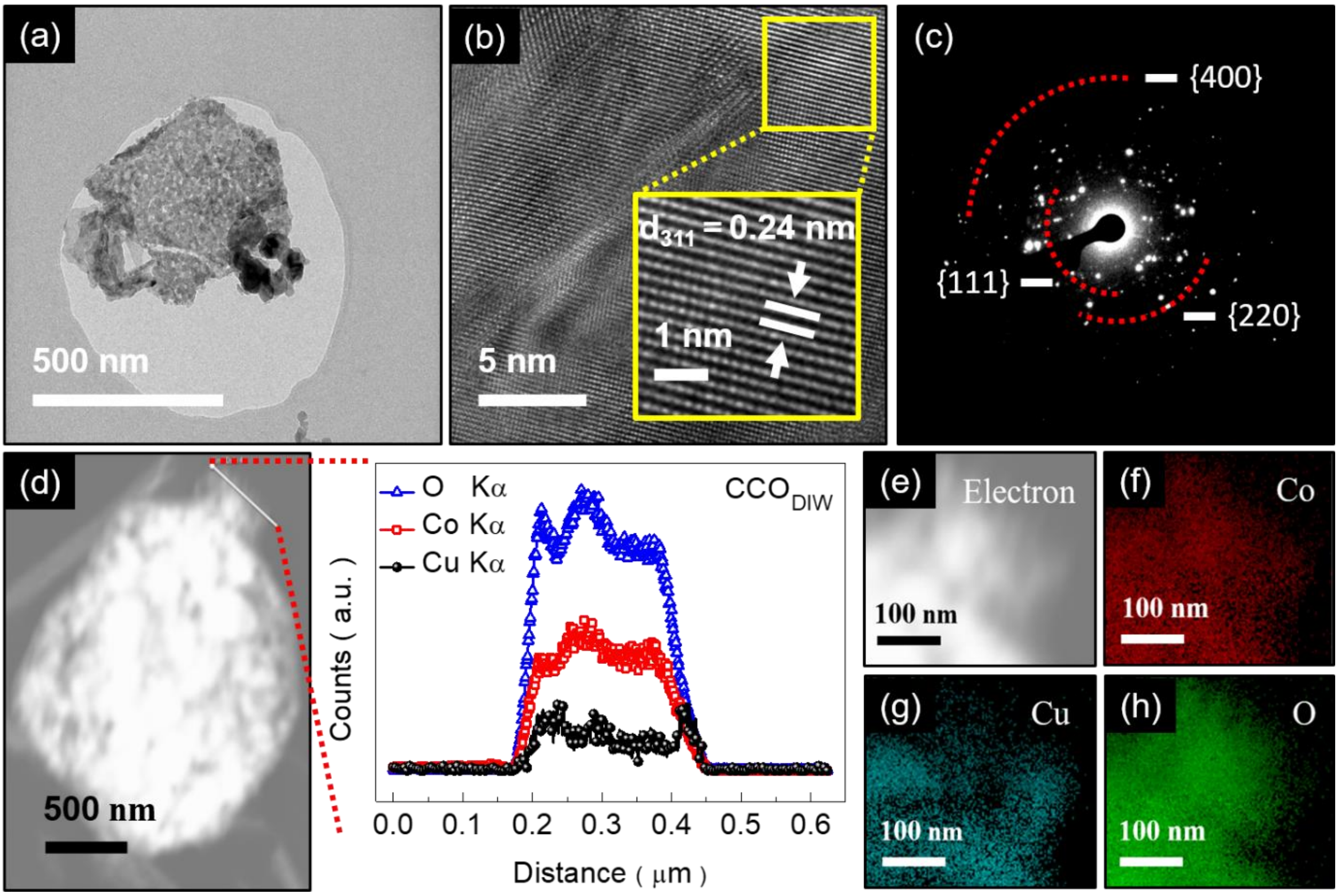

Figure 5. (a) Transmission electron microscopy (TEM) image of the $CuCo_2O_4$ (CCO) film synthesized with deionized water (DIW) as solvent (CCO_{DIW}). The inset shows a field–emission scanning electrom microscopy (FE–SEM) image of the nanosheets; the nanopores on their surface are clearly visible and correspond to the white spots in the TEM image. (b) High–

resolution TEM image of the CCO_{DIW} film and an enlarged view (yellow box) showing the visible lattice fringe pattern that corresponds to the d_{311} lattice plane of $CuCo_2O_4$. (c) Selected–area electron diffraction image; the {400}, {220}, and {111} reflections arose from the polycrystalline nature of the CCO_{DIW} nanosheets. (d) Eenegy dispersive spectroscopy (EDS)–scanning TEM (STEM) image with a line scan chemical mapping (right side image) of the CCO_{DIW} nanosheets. EDS–STEM chemical mapping of the CCO_{DIW} nanosheets: (e) EDS–STEM electron image and (f) Co, (g) Cu, and (h) O distribution.

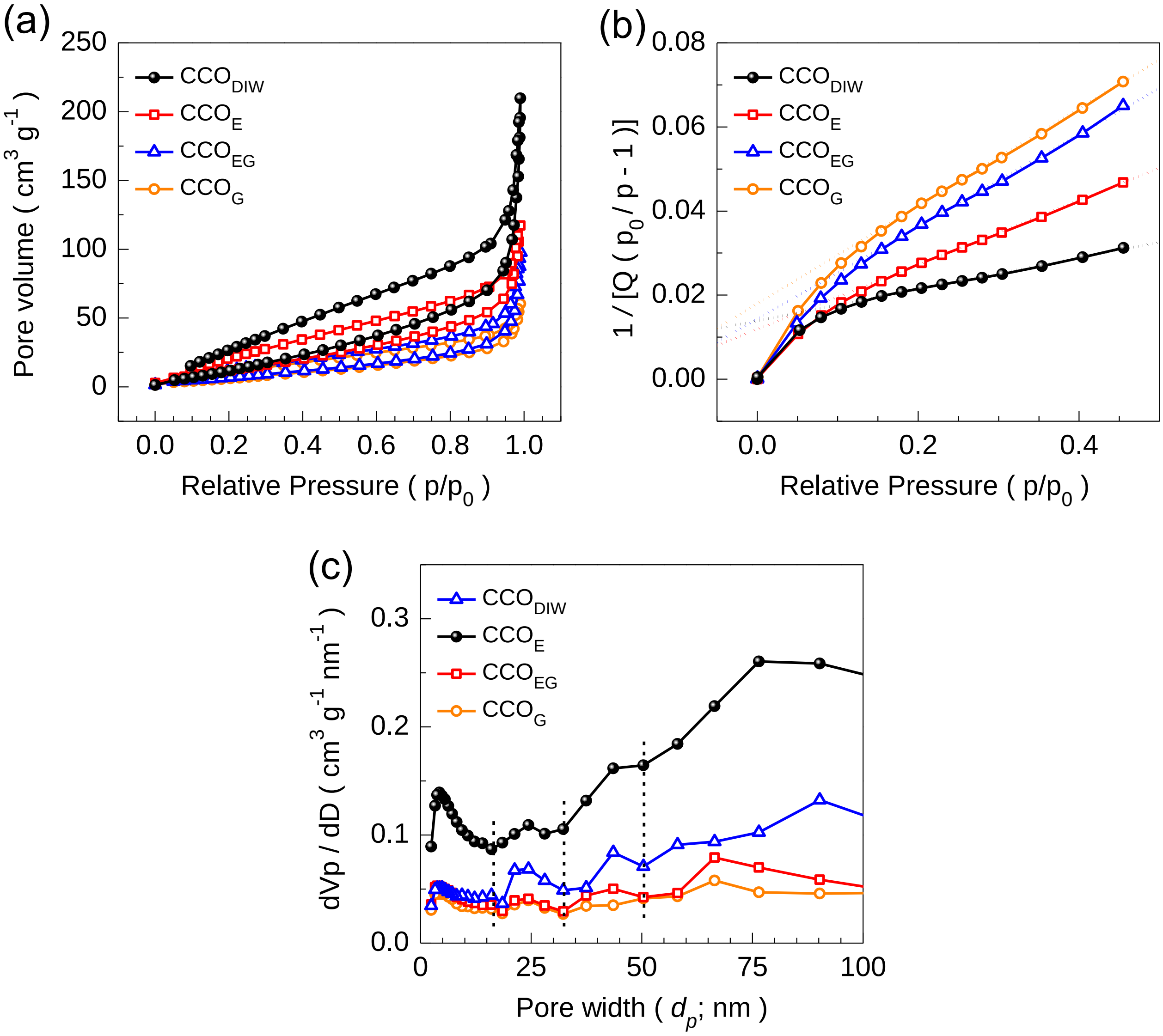

Figure 6. (a) N_2 adsorption and desorption isotherm curves, (b) Brunauer–Emmett–Teller specific surface area plots and (c) pore diameter distribution of the $CuCo_2O_4$ (CCO) samples, synthesised with various solvents (DIW: deionized water; E: ethanol; EG: ethylene glycol; G: glycerol).

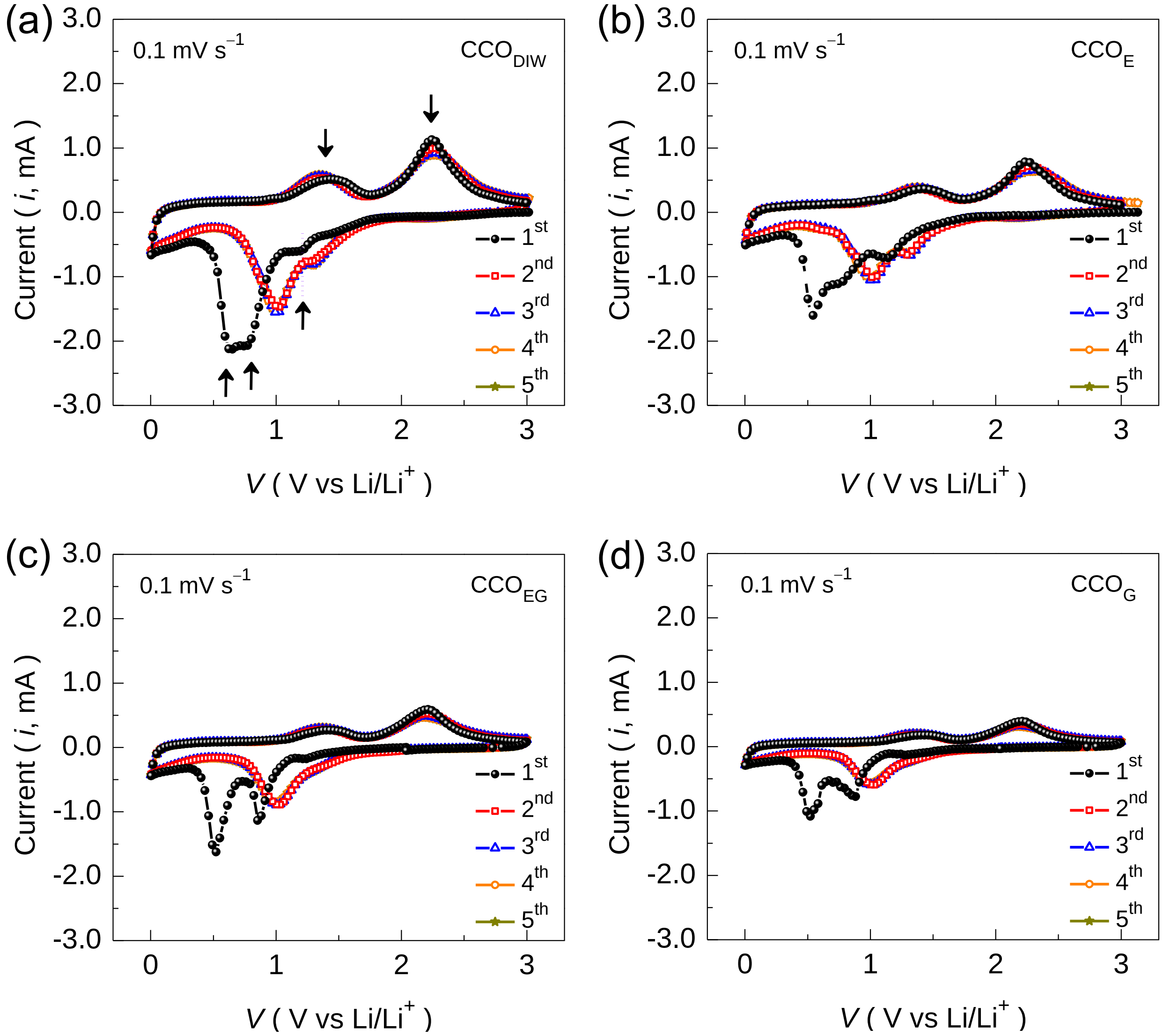

Figure 7. (a) Initial five cyclic voltammetry (CV) cycle curves, at a scan rate of 0.1 mV s^{-1}, of the $CuCo_2O_4$ (CCO) anodes synthesized with (a) deionized water (DIW), (b) ethanol (E), (c) ethylene glycol (EG), and (d) glycerol (G).

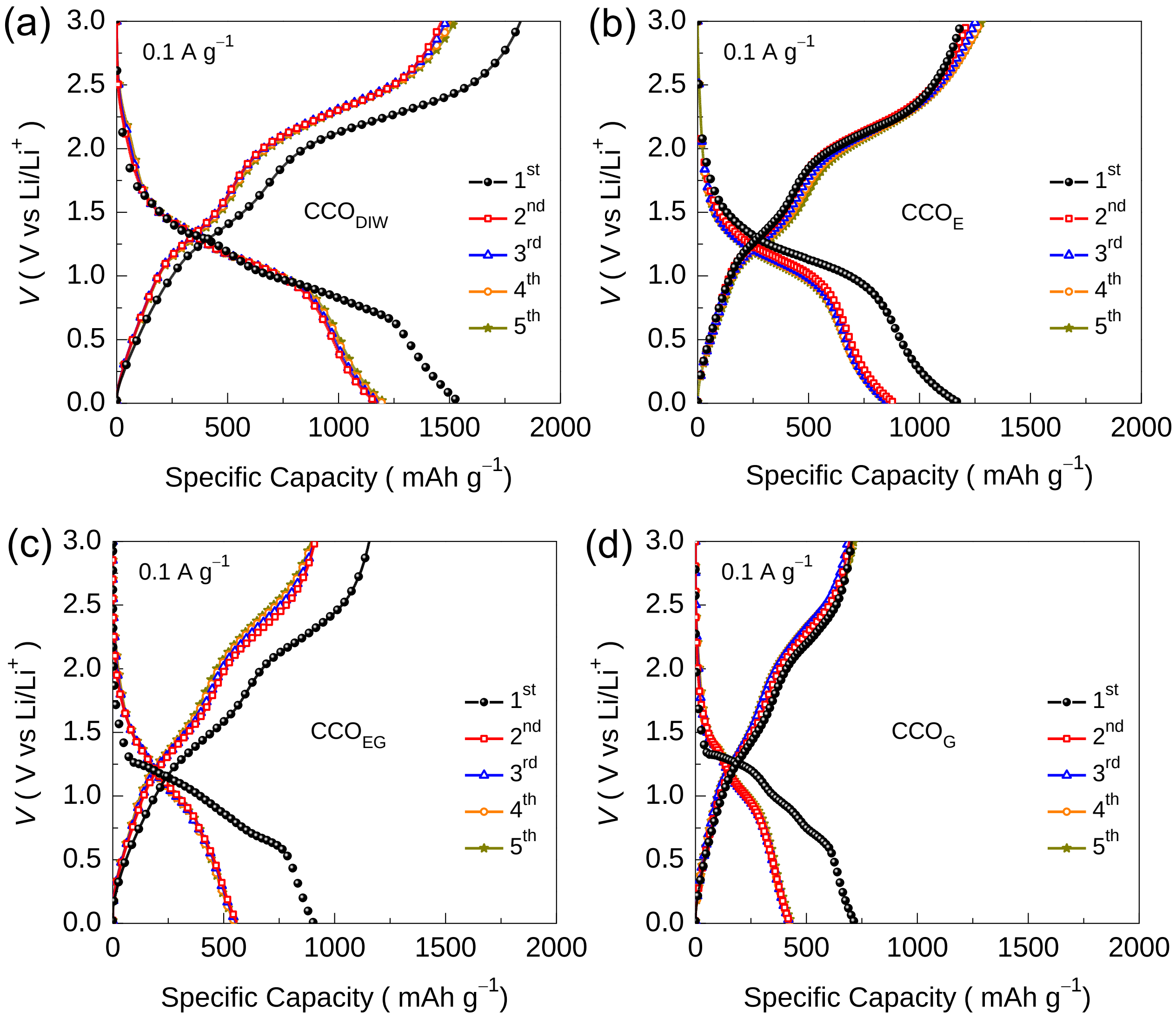

Figure 8. (a) Initial discharge–charge curves, at a current density of 0.1 A g^{-1}, of the $CuCo_2O_4$ (CCO) anodes synthesized with (a) deionized water (DIW), (b) ethanol (E), (c) ethylene glycol (EG), and (d) glycerol (G).

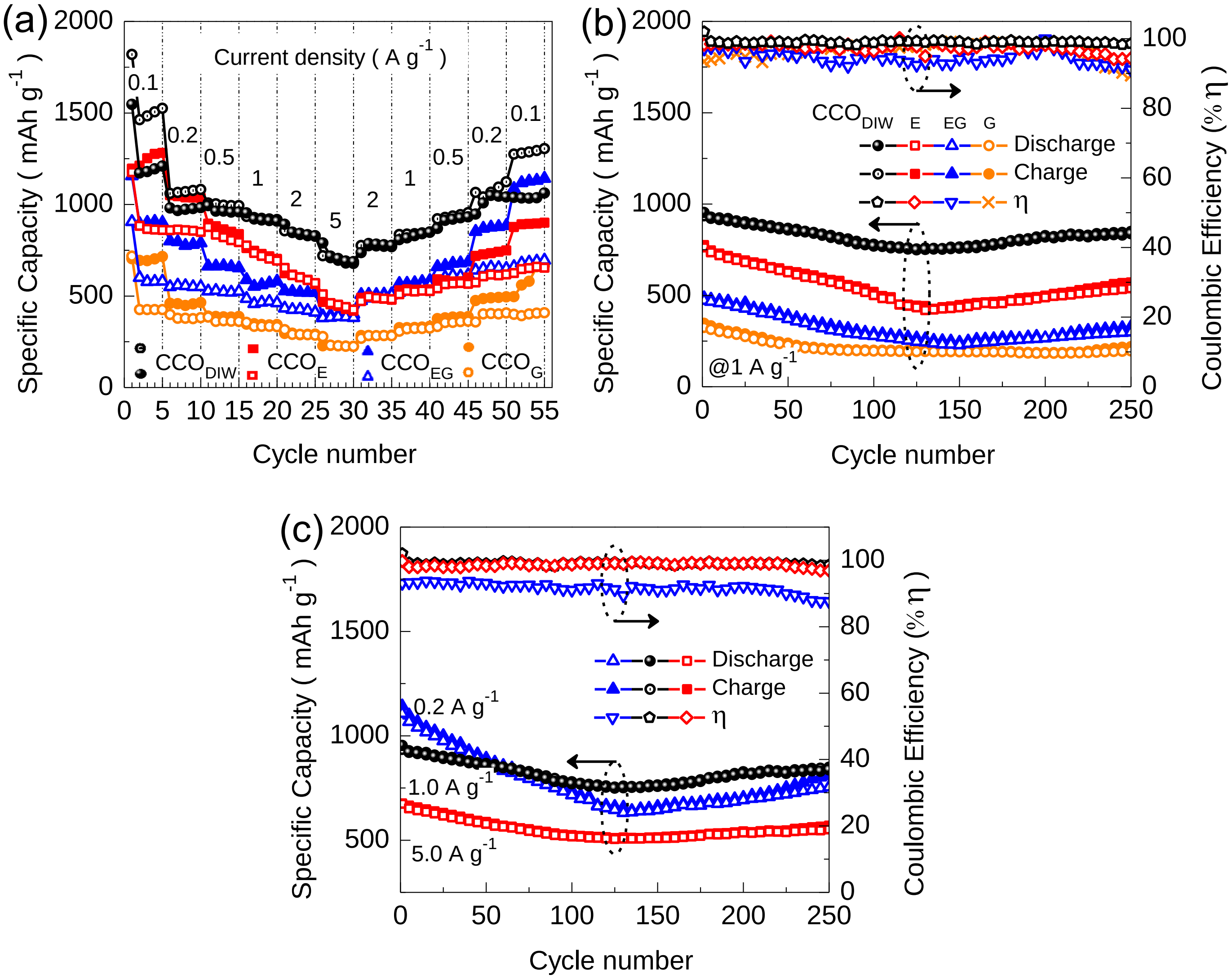

Figure 9. (a) Current density–dependent specific capacity, i.e., restoration capability, from 0.1 to 5.0 A g^{-1} for $CuCo_2O_4$ (CCO) anodes synthesized with deionized water (DIW), ethanol (E), ethylene glycol (EG), and glycerol (G) (open and filled symbols represents the discharge and charge capacities for all the anodes except the CCO$_{DIW}$ one, filled sphere represents discharge

and open sphere stands for charge capacity). (b) 250 discharge–charge cycle stability and coulombic efficiency at 1.0 A g^{-1} for the various anodes. (c) Cycle stability of the mesoporous CCO_{DIW} nanosheet anode at different current densities.

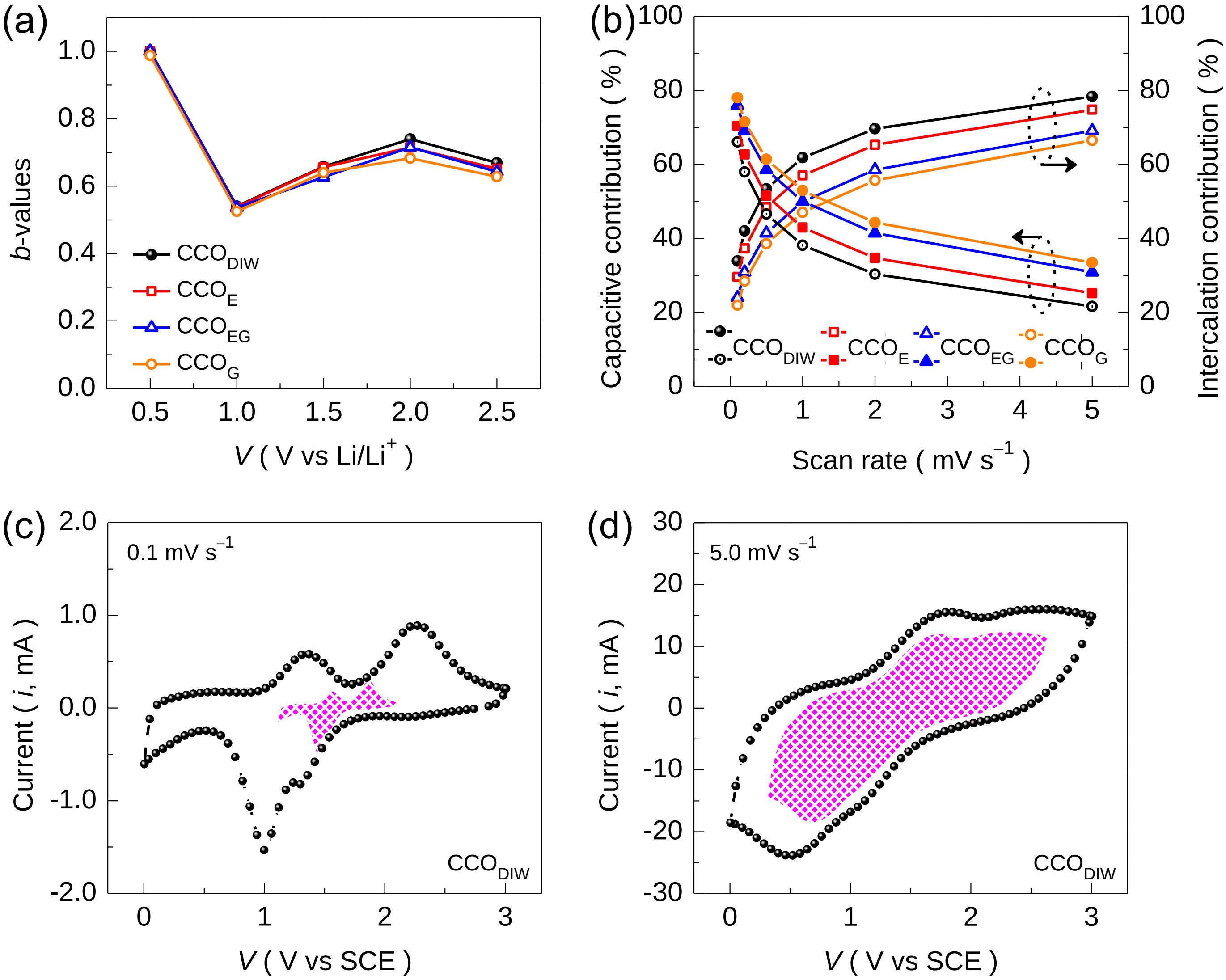

Figure 10. (a) *b*–values (slope of the log(*i*) vs. log(*v*) plots, where *i* is the current response) as a function of the cyclic voltammetry (CV) potential for cathodic sweeps and (b) the corresponding scan–rate dependent relative capacitive and diffusive capacity contribution for $CuCo_2O_4$ (CCO) anodes. CV response for the mesoporous nanosheet anode, synthesised with

deionised water (CCO_{DIW}), at (c) 0.1 and (d) 5 mV s^{-1}; the black spheres (total current) represents experimental values, while the interface and surface capacitive contribution currents (shaded regions) were determined from the data in Figure S3 (Supplimentary Information).

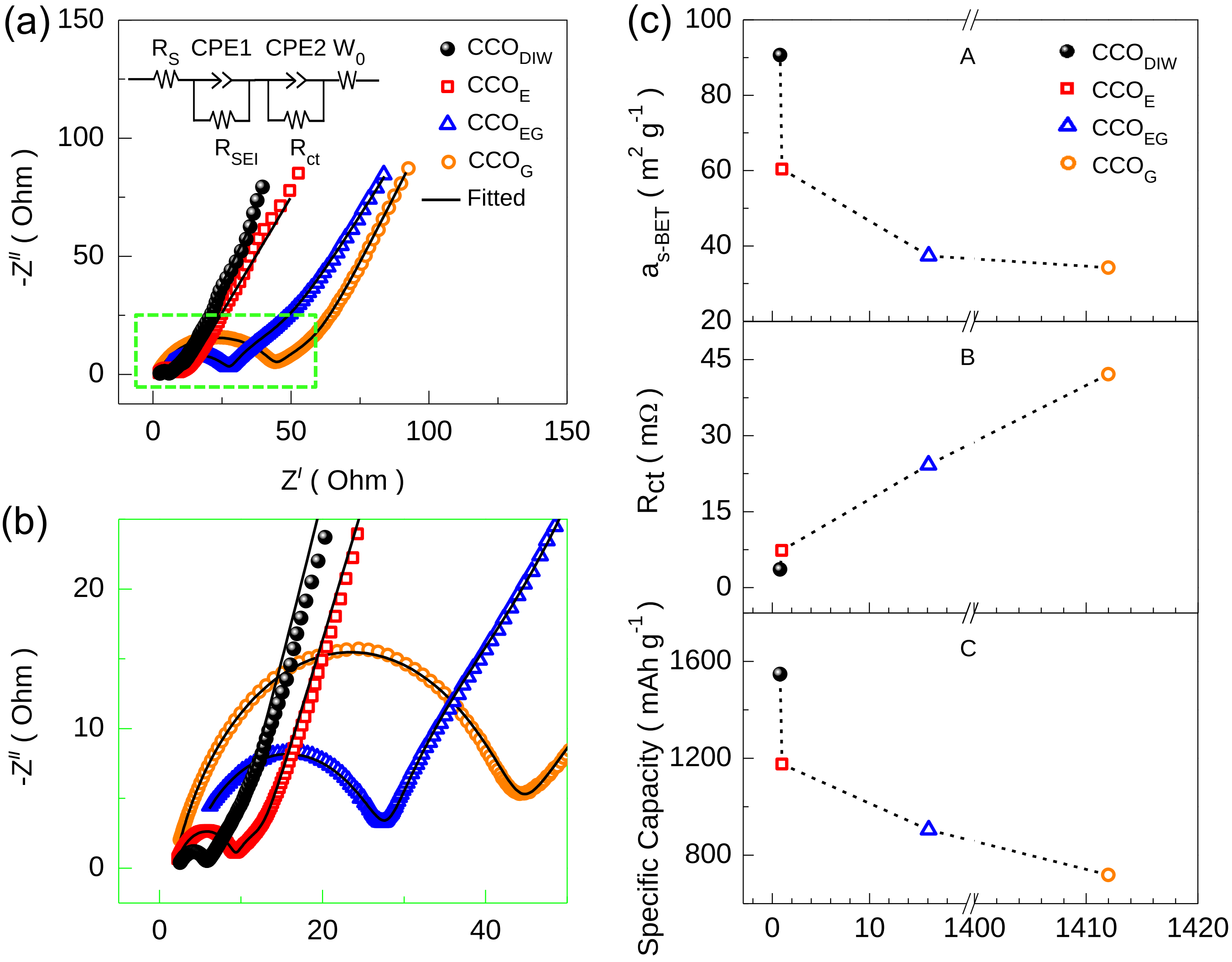

Figure 11. (a) Nyquist plots along with an equivalent fitted circuit; the fitted curves overlapped

the experimental results and semicircle nature of the electrochemical impedance spectroscopy curves is highlighted in (b). (c) Brunauer–Emmett–Teller specific surface area ($a_{s\text{–}BET}$, A), charge transfer resistance (Rct, B), and specific capacity (C) as a function of the solvent viscosity for the $CuCo_2O_4$ (CCO) anode synthesized with deionized water (DIW), ethanol (E), ethylene glycol (EG), and glycerol (G).

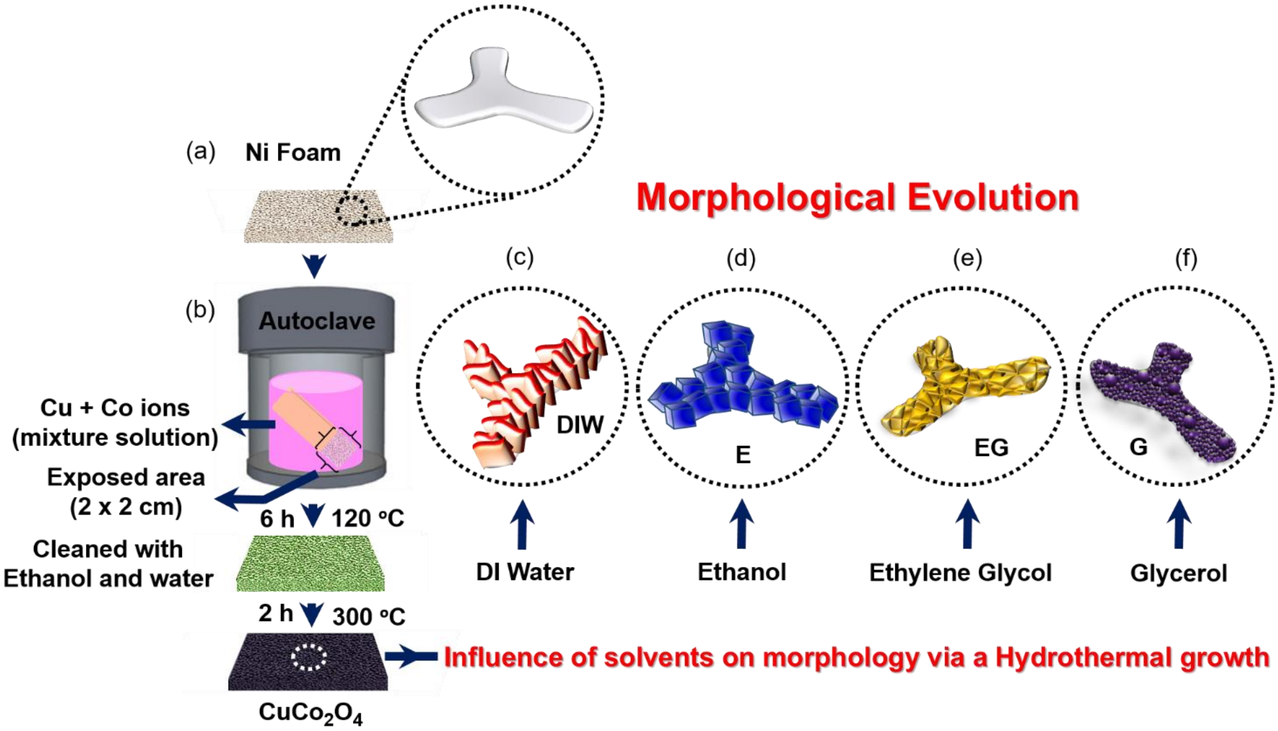

Figure 12. Schematic of the experimental procedure for the $CuCo_2O_4$ shape control via a mild hydrothermal technique. (a) Pre–cleaned Ni foam substrate with a smooth surface. (b) Heating and successively annealing of the pre–cleaned Ni foam and Cu/Co ions mixture solution in a Teflon–lined stainless steel autoclave. Morphological evolution associated with the different

solvents used for the hydrothermal synthesis: (c) mesoporous nanosheets (DI: deionized), (d) cubic structure, (e) compact granular, and (f) agglomerated spherical morphology. Each solvent had a different viscosity that varied with the reaction rate, resulting in different growth mechanism.